

Oxygen Permeability of Fully Condensed Lipid Monolayers

Mark A. Borden and Marjorie L. Longo*

Department of Chemical Engineering and Materials Science, University of California, Davis, California 95616

Received: December 11, 2003; In Final Form: March 10, 2004

The oxygen permeation resistance of highly condensed monolayers composed of a homologous series of saturated diacyl phosphatidylcholine lipids was measured using a novel technique that combined micromanipulation and electrochemical techniques. The use of lipid monolayer-coated air microbubbles allowed measurement of the oxygen permeation resistance of fully condensed lipid monolayers that were previously unavailable using classical film balance techniques. Fully condensed lipid monolayers were found to significantly impede oxygen transport from the gas core, an effect that increased with lipid acyl chain length. The magnitudes of the measured oxygen permeation resistances, 10^2 to 10^3 s/cm, agree with literature values for various gases permeating through highly condensed fatty acid and alcohol monolayers. Such high resistances can account for the previously observed hindered dissolution of lipid-stabilized microbubbles in degassed media. Additionally, the ability to probe a lipid monolayer in its fully condensed state leads to new physical insights into monolayer permeation.

Introduction

The permeation of gas molecules across highly condensed monolayers is of considerable interest for industrial applications as well as in the fields of environmental science and biophysics. Industrial applications include unit processes involving gas–liquid contact, such as gas absorption¹ and fermentation.² Environmental concerns include the ability of insoluble monolayers to retard evaporation in water reservoirs³ and the influence of natural surfactants and microbubbles on the transport of gases, salts, and organic material across the air–sea interface.^{4,5} Likewise, knowledge of gas transport through lipid monolayers provides valuable insight into the biophysics of passive transport through the plasma membrane.^{6,7}

Studies of gas penetration through insoluble monolayers go back almost eighty years to when Rideal⁸ and Langmuir⁹ first recorded the resistance of fatty acid monolayers to water evaporation. Langmuir and Schaefer¹⁰ developed an energy barrier theory for gas permeation based on their observations that resistance increased exponentially with carbon chain length and surface pressure and decreased exponentially with temperature. Subsequent experiments confirmed these general trends for the transport of water vapor and gases through monolayers of long-chain acids, esters, and alcohols.³ Blank developed an alternative model based on kinetic theory for gases and natural density fluctuations in the monolayer.^{11,12} Barnes developed a simple model based on the accessible area for penetration.^{13,14} Simple diffusion was discarded as a possibility for condensed monolayers due to the following:^{15,16} (i) partitioning effects are physically ambiguous because the size of the permeating species is of the same magnitude as the monolayer molecule; (ii) the permeability values measured for monolayers compare to analogous values for solids; (iii) the apparent diffusivity increases with film thickness for a homologous series; (iv) the presence of inert gases (e.g., water vapor and nitrogen) causes a decrease in the permeability by as much as 2 orders of

magnitude. The energy barrier, density fluctuation, and accessible energy theories have been shown to account for much of the data.¹⁷

Several techniques have been employed to measure the gas permeability of condensed monolayers. Most experiments required an apparatus with a fixed liquid surface area, and excess monolayer material was applied to the surface in order to reach the maximum, or “equilibrium”, spreading pressure (Π_e).^{3,16} Note that monolayers may be in equilibrium at surface pressures less than Π_e but undergo a slow transition to a 3D bulk phase at higher surface pressures, although they are often metastable under states of compression and reach much higher surface pressures before collapse. The Langmuir–Schaefer technique for monitoring water evaporation, which utilizes the Langmuir trough to compress the monolayer to a known surface coverage and surface pressure, was adapted to gas permeation studies.¹⁸ More recently, Unwin et al. developed an electrochemical technique involving the use of an ultra-microdisk electrode (UME) in the aqueous subphase in conjunction with the Langmuir trough to measure the transfer kinetics of gases through monolayers at gas–liquid and liquid–liquid interfaces.^{19–21} This technique has been used to measure the oxygen permeability of fatty alcohol and phospholipid monolayers at the air–water and organic liquid–water interface.^{19–22} In this technique, the UME is translated in the aqueous medium to within several micrometers of the air–water interface and a potential is applied that causes the reduction of dissolved molecular oxygen. Pletcher and Sotiropoulos determined that a 25 μm diameter Pt UME maintained at ~ 0.5 V (vs reference electrode) in a stagnant aqueous medium is sufficient to fully reduce dissolved oxygen to form water via a diffusion-limited, four-electron-transfer reaction.^{23,24} The irreversible electrolysis of oxygen at the UME tip creates a concentration gradient that induces the transfer of oxygen from the gaseous phase. The current is followed as the tip approaches the interface at a rate slow enough to maintain steady state. The theoretical tip response is calculated by solving the diffusion equation in each phase with an internal boundary condition that accounts for the interfacial kinetics.^{19,25} In

* Corresponding author. E-mail: mllongo@ucdavis.edu. Tel: (530) 754-6348. Fax: (530) 752-1031.

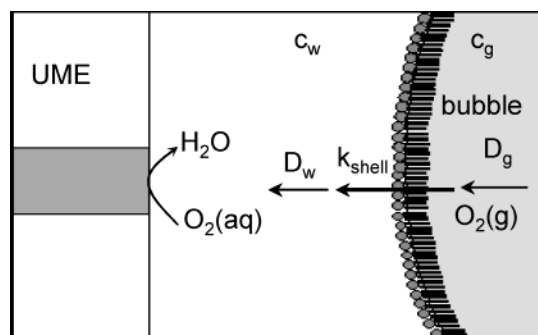


Figure 1. Principles of UME-induced transfer of molecular oxygen from the microbubble gas core to the UME tip. The transport resistance of the condensed state lipid shell limits the flux of oxygen.

principle, comparison of the experimental and theoretical steady-state current–distance profiles allows the estimation of the interfacial permeability, provided the bulk phase diffusivities and partition coefficients are known.

Most condensed monolayer permeation experiments were performed at or below the equilibrium spreading pressure of the monolayer species (~ 45 mN/m). The inherent difficulty of maintaining the monolayer in the metastable state at surface pressures greater than Π_e has made it difficult to measure the gas permeability of highly condensed monolayers (i.e., the solid phase), and only a few attempts have been made.^{20,26} The unlikely scenario of a highly condensed monolayer occurring at the air–water interface of a natural body of water made such measurements seem unnecessary.^{3,4} However, recent interest in natural and synthetic microbubbles has sparked a new desire for measurements of the gas permeability of highly condensed monolayers.

Lipid-coated microbubbles offer a unique system for studying fully condensed monolayers. Microbubbles are ubiquitous in nature and are thus important to many areas of fundamental and engineering science.⁵ Current applications of microbubbles in medicine include ultrasound contrast agents,²⁷ drug/gene delivery agents,²⁸ and blood substitutes.²⁹ Applications in industry include fermentation,³⁰ gas absorption,³¹ and microflotation.⁵ The study of naturally occurring stable microbubbles and the need for high stability microbubbles in medical and industrial applications have led to the development of facile techniques to coat micron-scale bubbles with an insoluble lipid monolayer. The monolayer coating stabilizes the microbubble against coalescence and rapid dissolution and has been reported to stabilize air microbubbles for days to weeks.^{5,32} The unusually high stability has been attributed to the variable permeability and elasticity of the organic shell.^{33,34} The Laplace pressure in the gas core drives dissolution until the lipid monolayer is fully condensed. In the fully condensed state, the shell provides maximum resistance to gas permeation^{35,36} and has essentially zero surface tension.^{37,38} Once the bubble shell has become fully condensed, the driving force and kinetics of dissolution in an air-saturated media completely diminish and the bubble is stable indefinitely. To our knowledge, no previous attempts have succeeded at measuring the gas permeability of fully condensed monolayers.

Here we investigated the oxygen permeability of fully condensed monolayers that are attainable on lipid-coated microbubbles using a novel apparatus that incorporates electrochemical and micromanipulation methods (Figure 1). Individual preformed microbubbles and the UME were manipulated with a finely tuned micropipet apparatus to obtain current–distance profiles that allowed determination of the monolayer

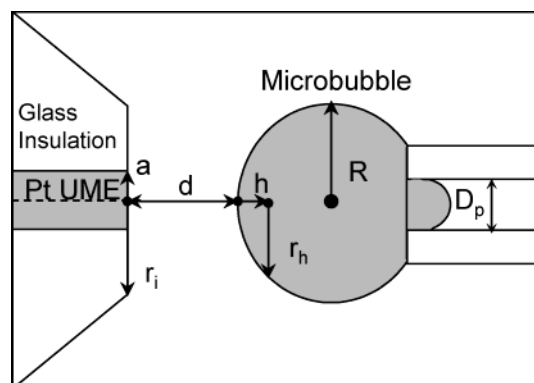


Figure 2. Important geometrical parameters for analyzing current–distance profiles.

shell permeability to oxygen (Figure 2). The oxygen permeability was measured as a function of the headgroup size for two single-chain surfactants and of tail chain length for a homologous series of phospholipids. Our results correlate very well with previous measurements of monolayer permeation, demonstrating the accuracy of this technique. The UME technique described here allows the direct measurement of the microbubble shell resistance to oxygen permeation for the first time. Thus, the results described here more appropriately and accurately describe the gas permeability of the lipid monolayer shell encasing a microbubble compared to other techniques such as bubble dissolution, where shell crumpling and experimental conditions deviate significantly from theory.

Experimental Section

Materials. Saturated phospholipids, 1,2-diacyl-*sn*-glycerol-3-phosphatidylcholine (diC-*n*-PC; $n = 16, 18, 20, 22, 24$), were purchased from Avanti Polar Lipids (Alabaster, AL). Emulsifier, polyoxyethylene 40 stearate (PEG40S), and 1-octadecanol were purchased from Sigma (St. Louis, MO). Supporting electrolyte (KCl), buffer components (KH_2PO_4 and K_2HPO_4), and the reference redox reagent ($\text{Fe}(\text{CN})_6\text{K}_3$) were purchased from EM Science (Darmstadt, Germany). HPLC grade chloroform was purchased from Fisher Scientific (Fair Lawn, NJ). Deionized water was purified to $18 \text{ M}\Omega\text{-cm}$ with a Barnstead Nanopure water system (Dubuque, IA).

Preparation of Microbubbles. Microbubble solutions were prepared as described previously.³⁵ Briefly, the lipid (90 mol %) and emulsifier (10 mol %), or 1-octadecanol (95 mol %) and emulsifier (5%), were co-dissolved in chloroform. The emulsifier, which promotes lipid dispersion and inhibits coalescence, is a necessary component in forming lipid-coated microbubbles. Chloroform was then dried off using nitrogen gas, and the surfactants were resuspended in purified water to a lipid concentration of 3 mg/mL via bath sonification with heat for 20 min. Microbubbles were then formed via high-power tip sonification at the air–water interface and immediately cooled under cold tap water.

Apparatus and Procedure. The following important parameters shown in Figure 2 are used to define the UME setup: a is the radius of the electrode tip; d is the separation distance between the electrode tip and the microbubble surface; R is the microbubble radius; D_p is the diameter of the holding pipet ($\sim 100 \mu\text{m}$); and h and r_h are geometrical parameters used to measure the relative curvature of the bubble surface. The computer-controlled electrochemical analyzer (model CHI1205) with supporting software, glass cell, and electrodes with polishing supplies were purchased from CH Instruments (Austin,

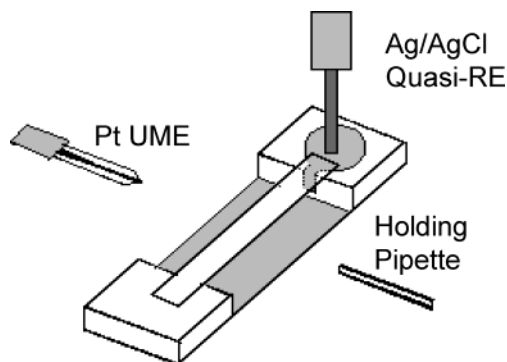


Figure 3. Top view of UME chamber (not to scale) showing relative placement of the working electrode (Pt UME), Ag/AgCl quasi-reference electrode, and holding pipet.

TX). The electrodes included two 25 μm diameter Pt UME's ($RG = r_i/a = 10$), two Ag/AgCl reference electrodes (RE), and a Pt wire counter electrode (CE). The reference electrodes were stored in 3.0 M KCl between experiments. Polished UMEs were tested for accuracy via cyclic voltammetry using the glass cell with an aqueous solution of 0.5 mM $\text{Fe}(\text{CN})_6\text{K}_3$ and 0.1 M KCl. An aqueous solution of 0.1 M KCl (supporting electrolyte) and 0.035 M KH_2PO_4 /0.042 M K_2HPO_4 (pH 7.0 buffer to counter evolving hydroxide ions) was used in all experiments entailing the reduction of molecular oxygen.²² Cyclic voltammetry results confirmed that a potential of -0.55 V applied to the UME (vs RE) was sufficient to completely reduce oxygen; higher voltages (about -0.7 V) resulted in the breakdown of buffer components.^{19,22} The steady-state current intensity (i_∞) at infinite separation was determined at various dissolved oxygen concentrations, including saturation. Dissolved oxygen fraction (compared to saturation at 1 atm) was controlled by vigorously stirring 50 mL of buffer solution for 1 h under regulated vacuum pressure.

Experiments entailing the UME-induced transfer of oxygen through the individual shells of preformed microbubbles were done in the chamber shown in Figure 3. The chamber consisted of two Teflon spacers sandwiched between two rectangular glass coverslips. The coverslips were coated with SurfaSil (Pierce, Rockford, IL) in order to make them hydrophobic. The result was a rigid chamber with an open transparent rectangular cavity of about 3 mL (Figure 4). The aqueous buffer was held stationary between the coverslips via surface tension. The UME chamber was placed on the stage of an inverted Nikon Eclipse TS-100 microscope equipped with infinity-corrected optics (experiments were performed in bright field), a high-resolution CCD camera (Dage MTI, Michigan City, IN), and a Super VHS recorder (JVC SR-VS20). Both the counter electrode and reference electrode leads were fastened from the electrochemical analyzer to the Ag/AgCl RE to make the quasi-RE used in the two-electrode configuration.^{19,20,22} The quasi-RE was placed in the well of the Teflon spacer as shown in Figure 3. The UME and holding pipet were controlled with apposing micromanipulators (model MHW-3, Narishige, Japan) mounted on adjustable orbital stages (Meridian, Kent, WA). The procedures for preparing the holding pipet and applying and measuring a suction pressure were followed as described previously.³⁹ Suction pressure was applied to the holding pipet to capture single preformed microbubbles ($R > r_i$) that were injected into the chamber via a syringe equipped with a wide bore needle. As shown in Figure 2, the micropipet/bubble interface was at the opposite side of the bubble with respect to the electrode and was thus unlikely to affect the measured shell permeability.

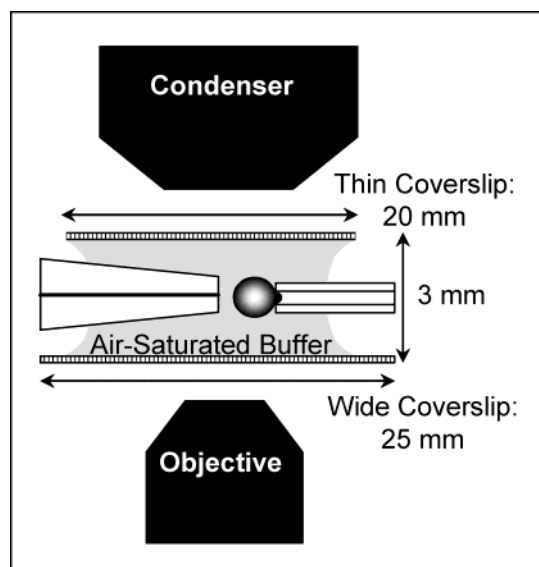


Figure 4. Side view (not to scale) of UME chamber showing dimensions of chamber and arrangement of optics.

Alternatively, in some experiments, single microbubbles were captured by adhering them to a small dab of vacuum grease applied to the micropipet tip. The resulting shell permeability values were found to be independent of holding technique within experimental error. Use of the fine grain manipulators enabled the centering of the UME tip with respect to the bubble surface (Figure 4). The setup was shielded from background electrical interference by a Faraday cage. At least 30 repeats over three experiments (using both UME tips and reference electrodes and multiple solutions) were performed for each microbubble coating species. The steady-state current intensity was then measured as a function of the tip–bubble separation distance as the bubble was translated toward the UME ($0.2 < d/a < 6.0$) in discrete movements at 10–20 s intervals (Figure 5).

Analysis. Theoretical steady-state current–distance profiles were simulated and compared to experimental results in order to estimate the shell resistance to oxygen permeation. The theoretical profiles were simulated using the computer program developed by Unwin, Macpherson, et al. that employs the alternating implicit finite-difference method (ADIFDM) to calculate the time-dependent current response of the UME tip.^{19,25} Briefly, the time-dependent current response is calculated from the oxygen flux at the electrode tip, which, in turn, is determined by solving the diffusion equation in each phase, coupled by an internal boundary condition that accounts for the transport resistance of the interface, for arbitrary values for the diffusivities, bulk phase concentrations, and interfacial transport kinetics. Values for the bulk phase concentrations and diffusivities used in the simulations are given in Table 1.^{19,40,41} The shell resistance to oxygen permeation, R_{shell} (i.e., inverse interfacial transport coefficient), was varied as the single fitting parameter. Figure 6 shows the dependence of the theoretical normalized steady-state current intensity on R_{shell} at a separation of $d/a = 0.5$.

In the simulation, the surrounding aqueous medium was assumed to be oxygen saturated at radial distances from the electrode center greater than the radius of the glass insulation, which is valid for the case $RG > 10$.¹⁹ In addition, the air core of the microbubble served as an infinite source of oxygen. Simulation results showed that the high diffusivity and concentration of oxygen in the gas core relative to the aqueous phase cause the oxygen concentration in the gas core to be

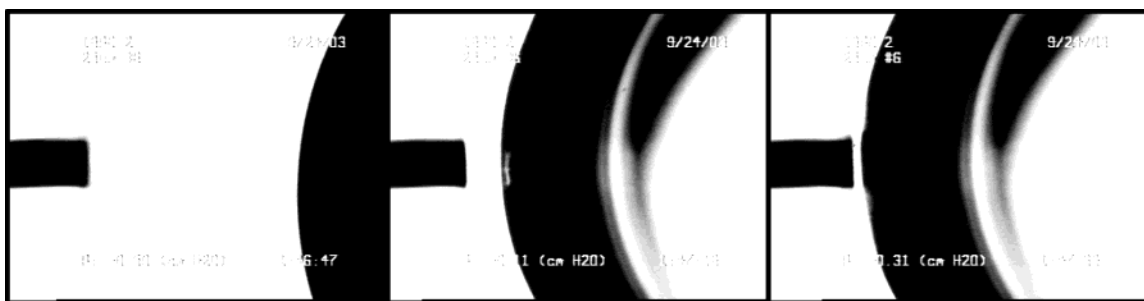


Figure 5. Videomicrographs showing typical approach of Pt UME to microbubble surface. Electrode diameter is 25 μm .

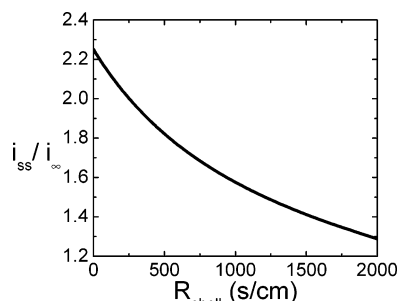


Figure 6. Simulated normalized steady-state current intensity at $d/a = 0.5$ versus interfacial transport resistance of the microbubble shell to oxygen permeation.

TABLE 1. Model Parameters

parameter	definition	value
c_w	bulk O_2 concentration in the aqueous phase	$2.17 \times 10^{-7} \text{ mol/cm}^3$
c_g	bulk O_2 concentration in the gas core	$8.59 \times 10^{-6} \text{ mol/cm}^3$
D_w	bulk O_2 diffusivity in the aqueous phase	$2.1 \times 10^{-5} \text{ cm}^2/\text{s}$
D_g	bulk O_2 diffusivity in the gas core	$0.2 \text{ cm}^2/\text{s}$

effectively uniform at its bulk value, even in the absence of an interfacial permeation resistance. Likewise, simulations showed that the amount of oxygen consumed by the UME during a typical experiment was less than 2% of the oxygen contained in the gas core ($R \geq 100 \mu\text{m}$).

The finite curvature of the bubble interface introduced a deviation from theory, which assumes an infinite planar interface, and thus the simulation might be expected to overestimate the current response (and hence the shell resistance). However, Fulian et al. recently used the boundary element method (BEM) to simulate the steady-state current–distance profile of a disk microelectrode approaching a spherically distorted substrate and determined that the current intensity was not significantly affected by values of r_h greater than $4a$ when $h = a$ (see Figure 2).⁴² As stated above, the bubbles used in this study had a radius greater than the radius of the insulation on the microelectrode ($RG = 10$), and thus the value of r_h was greater than $4.5a$ at $h = a$. Therefore, the simulation was expected to correctly model the experimental system, at least for small separations ($d/a < 1$).

Results and Discussion

Dissolved Oxygen Measurement. The steady-state current at infinite separation (i_∞) was measured at various dissolved oxygen fractions to test the UME response and determine the apparent dissolved oxygen concentration in the buffer solution at saturation (Figure 7). Degassing under controlled vacuum with the aforementioned conditions has been previously shown

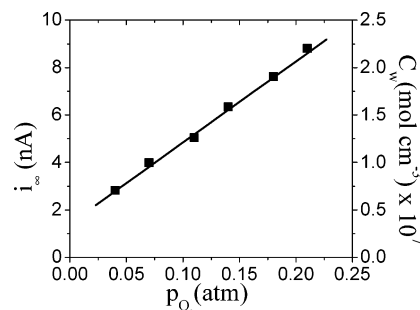


Figure 7. Steady-state current intensity at infinite dilution measured with 25 μm diameter UME and corresponding dissolved oxygen concentration calculated from eq 1 versus partial pressure of oxygen in the gas phase at equilibrium. Line is linear least-squares fit ($p < 0.0001$). Error bars were smaller than point size.

to yield the correct dissolved oxygen content.³⁵ The linear relationship between dissolved oxygen content and current response confirms the accuracy of the UME setup.^{24,35} The dissolved oxygen concentration (C_w) was calculated from the current response using the equation^{25,43}

$$i_\infty = 4nFaD_{\text{aq}}C_{\text{aq}} \quad (1)$$

where $n = 4$ electrons transferred per molecule,^{23,24} F is Faraday's constant, a is the electrode radius, and D_{aq} is the diffusivity of oxygen in the buffer ($2.1 \times 10^{-5} \text{ cm}^2/\text{s}$).^{20,40} The dissolved oxygen concentration under atmospheric conditions (C_{aq}) was thus determined to be $\sim 2.2 \times 10^{-7} \text{ mol/cm}^3$. This value is slightly below that measured for pure water ($2.7 \times 10^{-7} \text{ mol/cm}^3$), as would be expected for a saline solution.⁴⁴

Current–Distance Profiles. Normalized current–distance profiles were obtained for microbubbles coated with each monolayer species, including PEG40S, octadecanol, and diC16PC through diC24PC (Figure 8). The profiles were found to be independent of electrode combination and microbubble holding method (i.e., vacuum grease did not intercalate into the monolayer and affect permeability). In all cases, the current intensity increased dramatically as the UME approached the bubble surface. The resulting current–distance profiles were identical when approaching the same bubble five times, and the bubble diameter remained constant during the experiment. This experimentally confirms the assumption that the gas core was essentially an infinite oxygen source. As shown in Figure 8A, the current–distance profiles converged and showed good agreement with theory at small tip–bubble separations (i.e., $d/a < 1$). The normalized current intensity (i_{ss}/i_∞) for each microbubble was determined at $d/a = 0.5$ for comparison to the simulation results presented in Figure 6. Typical current–distance profiles for each microbubble coating species are given in Figure 8B.

The current intensity obtained from bubbles coated with long-chain lipids, diC18PC through diC24PC, depended on both the

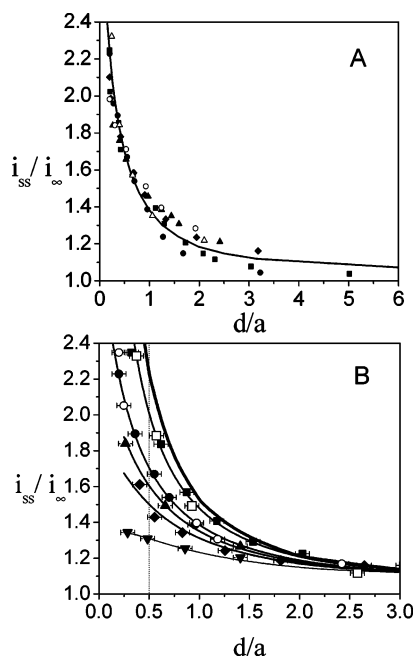


Figure 8. Typical normalized current profiles for fully formed microbubble shells. (A) Data points for diC18PC where $i_{ss}/i_{\infty} = 1.7$ at $d/a = 0.5$ (scatter for 6 experiments) and simulation results (line). (B) Current profile as a function of lipid acyl chain length: (□) PEG40S, (○) 1-octadecanol, (■) diC16PC, (●) diC18PC, (▲) diC20PC, (◆) diC22PC, (▼) diC24PC, (—) simulation with no interfacial resistance, (---) simulation fit to data.

age and position of the particular sample of bubbles prior to extraction from the foam layer and injection into the UME chamber (Figure 9). Figure 9A shows that, on average, recently formed lipid monolayer-coated bubbles (<2 h) that were extracted from the middle of the foam layer produced relatively high current intensities (i.e., low permeation resistances); the current profiles were similar to those obtained with microbubbles coated with pure PEG40S emulsifier. Figure 9B shows that, on average, microbubbles that were allowed to age (2–24 h) and were extracted from near the bottom of the foam layer had much lower current intensities (i.e., high permeation resistances); the current profiles were much lower than those obtained for microbubbles coated with pure PEG40S. The effect of age was expected, given that many of the larger bubbles (i.e., $R > 20 \mu\text{m}$) initially have a high area fraction of PEG40S-enriched expanded phase that is squeezed out over time due to surface-tension-driven dissolution of the gas core, resulting in a fully condensed lipid monolayer shell that stabilizes the bubble against further dissolution.³⁶ Likewise, size fractionation due to buoyancy effects and gas loss mechanisms, such as Ostwald ripening, are expected to cause bubbles near the bottom of the foam layer to shrink, and thus form fully developed shells, faster than those near the middle or top. The following results pertain primarily to fully developed shells.

Headgroup Effect. The effect of headgroup size was investigated by comparing the current response of microbubbles coated with PEG40S and octadecanol (Figure 8b). Both species have a single saturated 18-carbon hydrophobic tail; however, PEG40S, with its bulky headgroup, resists tight packing⁴⁵ and thus has a larger minimum area per molecule ($A_m \approx 40 \text{ \AA}^2/\text{molecule}$) than octadecanol ($A_m = 18\text{--}20 \text{ \AA}^2/\text{molecule}$).^{20,36,46} The larger area per hydrophobic chain under full compression for PEG40S provides more free volume through which oxygen molecules can penetrate. Accordingly, the current intensity was lower when approaching an octadecanol-coated microbubble

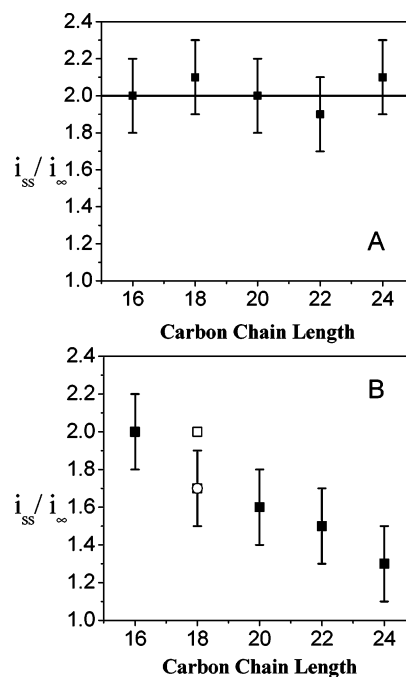


Figure 9. Normalized current intensity at $d/a = 0.5$ for undeveloped and fully formed microbubble shells versus chain length of carbon tail. (A) Data for undeveloped microbubbles (10–20 bubbles) extracted from middle of foam layer immediately after formation; line represents average value for PEG40S; points are mode and error bars are standard deviation. (B) Data for fully formed microbubbles (15–30 bubbles) from bottom foam layer 2–24 h after formation: (□) PEG40S, (○) octadecanol, (■) diC-*n*-PC; points are mode and error bars are standard deviation.

(open circles) compared to a PEG40S-coated microbubble (open squares). The normalized current intensities at $d/a = 0.5$ for PEG40S and octadecanol were 2.0 and 1.7, respectively, corresponding to R_{shell} values equal to 240 and 690 s/cm, respectively. These results clearly show that the smaller headgroup of octadecanol, which allows tighter packing of the hydrophobic chains, leads to a much higher resistance in the fully condensed state. The resistance of octadecanol is remarkably close to that obtained by Slevin et al. of $\sim 650 \text{ s/cm}$ for a planar octadecanol monolayer compressed on a Langmuir trough to very near the minimum area per molecule ($\sim 18.5 \text{ \AA}^2/\text{molecule}$).²⁰ The resistance of a fully formed PEG40S shell, however, is an order of magnitude higher than that obtained by Slevin et al. for a clean air–water interface ($\sim 10 \text{ s/cm}$).²⁰ Thus, the value of $\sim 200 \text{ s/cm}$ is the sum of resistances for the fully compressed PEG headgroup region and the disordered hydrophobic chain region.

Tail Chain Length Effect. The effect of the hydrocarbon tail chain length was tested for condensed phase monolayer-forming lipids (diC16PC through diC24PC). Undeveloped shells, which contain a high area fraction of emulsifier-enriched fluid phase,³⁶ and fully developed diC16PC shells behaved similarly to pure PEG40S (Figure 9A). The fully formed monolayer shells for the long-chain lipids, however, displayed a significant barrier to oxygen transport. Typical normalized current–distance profiles are shown in Figure 8. As expected, the current intensity (or, equivalently, the oxygen flux at the tip) decreased dramatically with increasing acyl chain length (Figures 8B and 9B). The resulting resistance values $R_{\text{oxygen}}^{\text{UME}}$ are given in Table 2 and shown in Figure 10. The value of $\ln[R_{\text{shell}}]$ increased considerably between diC16PC and diC18PC relative to the linear increase for diC18PC to diC24PC. The sharp transition between

TABLE 2. Shell Resistances

shell species	$R_{\text{oxygen}}^{\text{UME}}$ (s/cm)	$R_{\text{air}}^{\text{diss}}$ ^a (s/cm)
PEG40S	240	
octadecanol	690	
diC16PC	240	0
diC18PC	690	55 ± 53
diC20PC	910	140 ± 70
diC22PC	1180	260 ± 70
diC24PC	1950	310 ± 140

^a Calculated from eq 6, correcting for the wall effect and zero surface tension, using dissolution data of Borden and Longo.³⁵

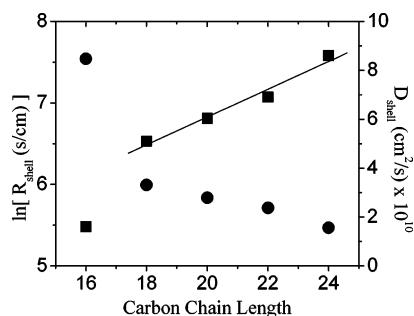


Figure 10. Shell permeation resistance, R_{shell} (■), and apparent diffusivity, D_{shell} (●), as a function of lipid acyl chain length. Line is linear least-squares fit to diC18PC through diC24PC ($p = 0.00183$).

diC16PC and diC18PC and the monotonic relationship for diC18PC through diC24PC are consistent with previous measurements of mechanical properties and observations of microbubble dissolution and lipid shedding behavior.^{35,37} The results for the homologous series demonstrate that the headgroup provides a negligible effect on the shell resistance in comparison to the hydrophobic tail groups for diC- n -PC where $n > 18$.

Interestingly, the shell resistance of diC18PC was equivalent to that of octadecanol (~ 690 s/cm). This result may be explained by considering the packing and orientation of the monolayer species in the microbubble shell. The hydrophobic tail groups of long-chain lipids and alcohols in the fully condensed state are perpendicular to the air–water interface and packed tightly in a hexagonal array.⁴⁷ The minimum area per chain for diC18PC measured on the Langmuir trough ($A_m = 18\text{--}20$ Å²/chain)^{36,48} is equivalent to that of octadecanol, and thus the lateral chain–chain separation is constant for the two species. The remaining parameter defining the free volume through which the permeating species must travel is the chain length, which is equal for diC18PC and octadecanol.

Monolayer Permeability. Our result for diC18PC also correlates well with previously published data of the interfacial transport coefficient versus surface coverage (Figure 11). Strutwolf et al. measured the oxygen transport coefficient (k) of adsorbed diC18PC monolayers that separated bulk aqueous and 1,2-dichloroethane (DCE) phases.²² Surface tension (σ) and transport kinetics were measured as a function of the lipid concentration in DCE (c) below the critical micelle concentration. Strutwolf et al.'s surface tension data were used by us to estimate the surface coverage using the Gibbs adsorption equation:⁴⁹

$$\Gamma = -\frac{c}{BT} \frac{d\sigma}{dc} \quad (2)$$

where Γ is the surface excess (mol/cm²), B is the gas constant, and T is temperature. The value for the derivative was determined by a linear least-squares fit to the plot of σ versus c , and the area per molecule (A) was then calculated from the

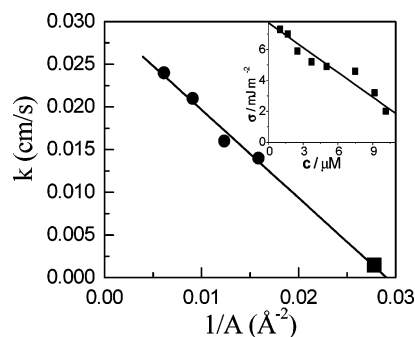


Figure 11. Oxygen transport coefficient through diC18PC monolayer versus reciprocal molecular area: (●) data from Strutwolf et al.²² and (■) microbubble shell permeability for diC18PC obtained in this study using the minimum area per molecule of 36 Å². Line is linear least-squares fit ($p = 0.00023$). Inset shows original data from Strutwolf et al. replotted as σ versus c with linear least-squares fit (slope = -1.87 ; $p < 0.001$).

surface excess at the concentrations used by Strutwolf et al. for the interfacial transport measurements (Figure 11, inset). The plot of k versus A^{-1} is linear, as has been observed previously for the permeation of oxygen²⁰ and bromine⁵⁰ through an octadecanol monolayer at the air–water interface. Also shown in Figure 11 is the value of the shell transport coefficient ($k_{\text{shell}} = 1/R_{\text{shell}}$) determined here for diC18PC at the minimum area per molecule ($A_m = 36$ Å²/molecule). The remarkable agreement between the measured value for the diC18PC microbubble shell and the linear trend obtained from the data of Strutwolf et al. demonstrates the usefulness of this method to measure the oxygen permeability of a fully condensed monolayer. The linear relationship between the transport coefficient and surface coverage was predicted by the simple accessible area model:^{17,20}

$$k = k_0 \left(1 - \frac{A_m}{A} \right) \quad (3)$$

where k_0 is the permeability of a clean interface. Extrapolation to zero surface coverage ($A^{-1} \rightarrow 0$) yields a value for k_0 that is 3 times lower than that measured for the clean air–water interface.²⁰ Furthermore, the measured value of k is not equal to zero for the fully condensed monolayer ($A \rightarrow A_m$). These results indicate that the accessible area theory alone is insufficient to account for oxygen permeation of condensed monolayers.

The exponential relationship between the shell resistance and lipid acyl chain length was predicted by the energy barrier model:^{3,17}

$$R_{\text{shell}} = R_0 \exp\left(\frac{E(n)}{BT}\right) \quad (4)$$

where R_0 is a frequency constant, $E(n)$ is the activation energy that depends on the number of carbons per chain (n), B is the universal gas constant, and T is temperature. It has been shown theoretically and experimentally that the cohesive energy of n -alkanes increases linearly with the addition of each methylene group to the carbon tail,⁵¹ and thus a linear increase in $E(n)$ with n is reasonable. An additional activation energy of ~ 100 cal/mol per CH₂ group per chain was determined from the slope of a linear least-squares fit of $\ln[R_{\text{shell}}]$ versus n for diC18PC through diC24PC (Figure 10), which is of the same order of magnitude as the value of ~ 190 cal/mol determined by Archer and La Mer for the permeation of water vapor through solid monolayers of fatty acids.²⁶

As discussed above, the linear trend between permeability and surface coverage is consistent with the simple accessible area model; however, there is significant deviation between experiment and theory at the extremes of minimum and maximum surface coverage. Lack of adequate values in the literature for the entropy of expansion of the fully condensed lipid monolayers used here precluded comparison of our data to the density fluctuation model.⁵² The energy barrier model adequately explains the relationship between resistance and chain length; however, it cannot be used to predict the monolayer resistance a priori from more fundamental parameters.¹⁵ Furthermore, none of these models account for the polycrystalline nature of the monolayer shell. A simple theory, perhaps one that combines the aforementioned models and additionally accounts for microstructure, would be of great value to aid in visualization of the physical process of gas permeation through condensed monolayers.

Permeation in macroscopic solids obeys simple diffusion theory (i.e., Fick's law) due to time averaging over many forward and backward jump events during the permeation process,⁵³ whereas permeation through the monolayer shell likely occurs in a single jump event.⁷ Although it is generally incorrect to directly compare macroscopic and sub-microscopic parameters, a rough order of magnitude comparison between the gas barrier properties of the lipid shell and bulk polymer materials may be valuable in gaining insight into the type of material most closely mimicked by the monolayer shell. The apparent shell diffusivity (D_{shell}) is calculated from the experimentally determined shell permeation resistance by the following relation:

$$R_{\text{shell}} = \frac{\delta}{D_{\text{shell}}} \quad (5)$$

where δ is the monolayer shell thickness. Note that partitioning into the monolayer is neglected when modeling gas permeation through condensed insoluble monolayers.^{7,12} The apparent shell diffusivity was found to be on the order of $\sim 10^{-10}$ cm²/s using a CH₂–CH₂ separation of 0.127 nm to calculate the value of δ of each chain length (Figure 10).⁵¹ These diffusivity values fall in the range of those observed for thermoplastics at room temperature (e.g., $D \approx 10^{-7}$ cm²/s for high-density polyethylene) and heated window glass (e.g., $D \approx 10^{-11}$ cm²/s for sintered alumina at 1700 °C).^{53,54} The tail region of the lipid monolayer is chemically similar to polyethylene; however, the inherent physical constraints of the monolayer shell of a microbubble cause it to be much more condensed. The hydrophobic effect confines the molecular orientation of the lipids such that the tail groups face the gas core while the headgroups face the aqueous phase. Laplace pressure effects act to further constrain the monolayer by forcing it to be fully compressed. In contrast, bulk polyethylene is generally free to relax, resulting in a greater inherent free volume for permeation.

The permeability of gases through solids has often been related to the material shear viscosity.⁵³ The sharp decrease in D_{shell} between diC16PC and diC18PC and the monotonic decrease in D_{shell} with carbon chain length between diC18PC and diC24PC are thus consistent with the mechanical property measurements reported recently by Kim et al. that show an increase in surface shear viscosity with chain length in similar microbubble shells.³⁷ Interestingly, Kim et al. also determined that the equivalent bulk shear viscosity of the polycrystalline lipid monolayer shell is similar in magnitude to heated window glass or plastic.

Microbubble Dissolution. Previously, we developed a modification to the Epstein and Plesset equation for bubble dissolution⁵⁵ that takes into account the gas permeation resistance of the shell in order to explain the remarkable stability of lipid monolayer-coated microbubbles.³⁵

$$-\frac{dR}{dt} = \frac{H}{R_{\text{shell}} + \{R/D_w\}} \frac{1 - f + \{2\sigma/P_a R\}}{1 + \{4\sigma/3P_a R\}} \quad (6)$$

where f is the ratio of vacuum pressure used to degas the surrounding medium over the ambient pressure (P_a) and H is the partition coefficient between air and water. Using the bubble dissolution data of Borden and Longo, while applying the empirical correction factor of 0.69 to D_w to account for the effect of the impermeable glass wall^{56,57} and the assumption of zero surface tension,³⁷ the apparent resistance of the lipid shell to air $R_{\text{air}}^{\text{diss}}$ was determined as the single fitting parameter, and the resulting values are listed in Table 2 alongside those measured in this study. The apparent resistances determined from the dissolution data $R_{\text{air}}^{\text{diss}}$ are lower than those determined with the UME tip near the microbubble surface in air-saturated media, $R_{\text{oxygen}}^{\text{UME}}$. Considering the differences between the diffusing species (N₂/O₂ vs O₂) is not sufficient to explain the discrepancy between the two data sets, as the resistance should be approximately equal in magnitude for the two nonpolar molecules. One remarkable observation of lipid-coated microbubbles (diC17PC through diC24PC) dissolving in degassed medium was that the shell crumples quite significantly and then restores sphericity in cycles. This observation is counter to the assumption of a quasi-static spherical shell used in deriving eq 6. The excess area, geometrical anomalies, and convection generated by the crumpling shell would cause the overall mass transfer rate to be higher than that predicted using the resistances measured in this study with the UME directly in eq 6.⁵⁸ Thus, the value of $R_{\text{air}}^{\text{diss}}$ is actually an empirical measure of the overall shell resistance that depends not only on the inherent permeability of the fully condensed monolayer but also on the particular crumpling and shedding events undergone by the bubble during dissolution. This would indicate that $R_{\text{air}}^{\text{diss}}$ for diC17PC through diC24PC depends on the rate of dissolution, and thus on the content of dissolved air (f). A systematic study of the effects of f and microstructure on $R_{\text{air}}^{\text{diss}}$ would be valuable to further address this issue.

Conclusions

We developed a novel apparatus employing electrochemical and micromanipulation techniques to measure the oxygen permeability of fully condensed monolayers at the air–water interface of microscopic bubbles. The accuracy of this technique was demonstrated in the excellent agreement between the permeation resistances measured here for octadecanol and diC18PC and previously reported values. The power of this technique was demonstrated in the ability to measure the gas permeability of fully condensed monolayers, which are extremely difficult to achieve on conventional flat troughs. This technique is more suitable for measuring the lipid shell permeation resistance to low molecular weight gases than previously described bubble dissolution methods, which deviate significantly from theory. The exponential relationship between permeation resistance and acyl chain length is accounted for using the energy barrier theory. The data also fit the linear trend for permeability versus surface coverage predicted by the accessible area model, although problems arise at the maxima

of surface coverage. The high gas barrier properties of fully condensed shells composed of long-chain lipids are sufficient to explain the relative stability of lipid-coated microbubbles in degassed media.

Acknowledgment. The authors would like to thank Dr. Julie Mcpherson and Prof. Patrick Unwin of the Department of Chemistry at the University of Warwick, UK, for kindly donating the computer code used to solve the two-phase transport problem. This work was funded by the Center for Polymeric Interfaces and Macromolecular Assemblies (Grant NSF DMR 0213618) and the Office of Naval Research Hydromechanics Division (Grant N000140310947). We are very grateful to Joe and Essie Smith for endowing part of this work.

References and Notes

- (1) Vazquez, G.; Antorrena, G.; Navaza, J. M. *Ind. Eng. Chem. Res.* **2000**, *39*, 1088.
- (2) Bredwell, M. D.; Srivastava, P.; Worden, R. M. *Biotechnol. Prog.* **1999**, *15*, 834.
- (3) *Retardation of Evaporation by Monolayers: Transport Processes*; La Mer, V. K., Ed.; Academic Press: New York, 1962.
- (4) Thibodeaux, L. J. *Environmental Chemodynamics—Movement of Chemicals in Air, Water and Soil*, 2nd ed.; John Wiley & Sons: New York, 1996.
- (5) D'Arrigo, J. S. *Stable Gas-in-Liquid Emulsions: Production in Natural Waters and Artificial Media*; Elsevier Science: New York, 1986; Vol. 40.
- (6) Gennis, R. B. *Biomembranes*; Springer-Verlag: New York, 1989.
- (7) Blank, M.; Britten, J. S. Physical principals in monolayer and membrane permeation. Coral Gables Conference on Physical Properties of Biological Membranes, 1968, Miami, FL.
- (8) Rideal, E. K. *J. Phys. Chem.* **1925**, *29*, 1585.
- (9) Langmuir, I.; Langmuir, D. B. *J. Phys. Chem.* **1927**, *31*, 1719.
- (10) Langmuir, I.; Schaefer, V. J. *J. Franklin Inst.* **1943**, *235*, 119.
- (11) Blank, M. *J. Phys. Chem.* **1964**, *68*, 2793.
- (12) Blank, M.; Britten, J. S. *J. Colloid Sci.* **1965**, *20*, 789.
- (13) Barnes, G. T.; Quickenden, T. I.; Saylor, J. E. *J. Colloid Interface Sci.* **1970**, *33*, 236.
- (14) Barnes, G. T. *J. Colloid Interface Sci.* **1978**, *65*, 566.
- (15) Blank, M. *J. Phys. Chem.* **1962**, *66*, 1911.
- (16) Barnes, G. T. *Adv. Colloid Interface Sci.* **1986**, *25*, 89.
- (17) Barnes, G. T. *Colloids Surf. A* **1997**, *126*, 149.
- (18) Hawke, J. G.; Alexander, A. E. In *Retardation of Evaporation by Monolayers: Transport Processes*; La Mer, V. K., Ed.; Academic Press: New York, 1962; p 67.
- (19) Barker, A. L.; Macpherson, J. V.; Slevin, C. J.; Unwin, P. R. *J. Phys. Chem. B* **1998**, *102*, 1586.
- (20) Slevin, C. J.; Ryley, S.; Walton, D. J.; Unwin, P. R. *Langmuir* **1998**, *14*, 5331.
- (21) Zhang, J.; Strutwolf, J.; Cannan, S.; Unwin, P. R. *Electrochem. Commun.* **2003**, *5*, 105.
- (22) Strutwolf, J.; Zhang, J.; Barker, A. L.; Unwin, P. R. *Phys. Chem. Chem. Phys.* **2001**, *3*, 5553.
- (23) Pletcher, D.; Sotiropoulos, S. *J. Electroanal. Chem.* **1993**, *356*, 109.
- (24) Pletcher, D.; Sotiropoulos, S. *J. Chem. Soc., Faraday Trans.* **1995**, *91*, 457.
- (25) Unwin, P. R.; Bard, A. J. *J. Phys. Chem.* **1991**, *95*, 7818.
- (26) Archer, R. J.; La Mer, V. K. *J. Phys. Chem.* **1954**, *59*, 200.
- (27) Klibanov, A. L. Ultrasound contrast agents: Development of the field and current status. In *Contrast Agents II*; Krause, W., Ed.; Springer-Verlag: New York, 2002; Vol. 222, p 73.
- (28) Unger, E. C.; Hersh, E.; Vannan, M.; Matsunaga, T. O.; McCreery, M. *Prog. Cardiovasc. Dis.* **2001**, *44*, 45.
- (29) Van Liew, H. D.; Burkard, M. E. *FASEB J.* **1995**, *9*, 148.
- (30) Worden, R. M.; Bredwell, M. D. *Biotechnol. Prog.* **1998**, *14*, 39.
- (31) Kluytmans, J. H. J.; van Wachem, B. G. M.; Kuster, B. F. M.; Schouten, J. C. *Chem. Eng. Sci.* **2003**, *58*, 4719.
- (32) D'Arrigo, J. S.; Imae, T. *J. Colloid Interface Sci.* **1992**, *149*, 592.
- (33) Yount, D. E. *J. Acoustic Soc. Am.* **1979**, *65*, 1429.
- (34) Yount, D. E. *J. Colloid Interface Sci.* **1997**, *193*, 50.
- (35) Borden, M. A.; Longo, M. L. *Langmuir* **2002**, *18*, 9225.
- (36) Borden, M. A.; Pu, G.; Runner, G. J.; Longo, M. L. *Colloids Surf. B* **2004**, in press.
- (37) Kim, D. H.; Costello, M. J.; Duncan, P. B.; Needham, D. *Langmuir* **2003**, *19*, 8455.
- (38) Van Liew, H. D.; Raychaudhuri, S. *J. Appl. Physiol.* **1997**, *82*, 2045.
- (39) Ly, H. V.; Block, D. E.; Longo, M. L. *Langmuir* **2002**, *18*, 8988.
- (40) Himmelblau, D. M. *Chem. Rev.* **1964**, *64*, 527.
- (41) Bird, R. B.; Stewart, W. E.; Lightfoot, E. N. *Transport Phenomena*, 1st ed.; John Wiley & Sons: New York, 1960.
- (42) Fulian, Q.; Fisher, A. C.; Denuault, G. *J. Phys. Chem. B* **1999**, *103*, 4387.
- (43) Saito, Y. *Rev. Polarogr. Jpn.* **1968**, *15*, 177.
- (44) *CRC Handbook of Chemistry and Physics*, 84 ed.; Lide, D. R., Ed.; CRC Press: New York, 2003.
- (45) Majewski, J.; Kuhl, T. L.; Gerstenberg, M. C.; Israelachvili, J. N.; Smith, G. S. *J. Phys. Chem. B* **1997**, *101*, 3122.
- (46) Kwok, D. Y.; Tadros, B.; Deol, H.; Vollhardt, D.; Miller, R.; Cabrero-Vilchez, M. A.; Neumann, A. W. *Langmuir* **1996**, *12*, 1851.
- (47) Kaganer, V. M.; Mohwald, H.; Dutta, P. *Rev. Modern Phys.* **1999**, *71*, 779.
- (48) Phillips, M. C.; Chapman, D. *Biochim. Biophys. Acta* **1968**, *163*, 301.
- (49) Adamson, A. W.; Gast, A. P. *Physical Chemistry of Surfaces*, 6th ed.; John Wiley & Sons: New York, 1997.
- (50) Zhang, J.; Unwin, P. R. *Langmuir* **2002**, *18*, 1218.
- (51) Israelachvili, J. N. *Intermolecular and Surface Forces*, 2nd ed.; Academic Press: San Diego, 1992.
- (52) Bockman, D. D. *Ind. Eng. Chem. Fundamentals* **1969**, *8*, 77.
- (53) Shelby, J. E. *Handbook of Gas Diffusion in Solids and Melts*; ASM International: Materials Park, OH, 1996.
- (54) *Permeability and Other Film Properties of Plastics and Elastomers*; Plastics Design Laboratory: Norwich, NY, 1995.
- (55) Epstein, P. S.; Plesset, M. S. *J. Chem. Phys.* **1950**, *18*, 1505.
- (56) Liebermann, L. *J. Appl. Phys.* **1956**, *28*, 205.
- (57) Wise, D. L.; Houghton, G. *Chem. Eng. Sci.* **1968**, *23*, 1501.
- (58) Liao, Y. C.; Lee, D. J. *J. Pharm. Sci.* **1997**, *86*, 92.